Results in Optics 5 (2021) 100158

Contents lists available at ScienceDirect

Results in Optics

journal homepage: www.sciencedirect.com/journal/results-in-optics

Invited Article

Application of optical orbital angular momentum to rotation measurements

Luyi Wang [a,1], Jiantao Ma [a,1], Min Xiao [a,b,c], Yong Zhang [a,b,*]

[a] National Laboratory of Solid State Microstructures, College of Engineering and Applied Sciences, and School of Physics, Nanjing University, Nanjing 210093, China
[b] Collaborative Innovation Center of Advanced Microstructures, Nanjing University, Nanjing 210093, China
[c] Department of Physics, University of Arkansas, Fayetteville, AR 72701, USA

ARTICLE INFO

Keywords:
Optical orbital angular momentum
Rotation measurements
OAM spectrum analysis
OAM-mode interferometer

ABSTRACT

In recent years, the orbital angular momentum (OAM) of light with a central phase singularity composed of a specific topological charge has attracted increasing attentions. In addition to the wide range of applications of OAM in optical manipulations and optical communications, the special angular spatial structure of OAM offers irreplaceable advantages for use in rotation measurement. Because of the relationship between OAM and angular position, the azimuthal information of optical fields can be acquired via detection of OAM. Several techniques based on this concept have been proposed to sense objects remotely using their angular motion. This article introduces the applications of OAM in object orientation recognition, rotation sensing, small angle measurement and rotating object imaging.

1. Introduction

1.1. Origins of orbital angular momentum

Light wave possesses linear momentum and angular momentum (Speirits and Barnett, 2013). The angular momentum includes spin angular momentum (determined by the polarization) and orbital angular momentum (OAM, determined by the spatial phase distribution of the optical field) (Bazhenov et al., 1992). The OAM-carrying beam specifically has a spiral phase characteristic (Dennis et al., 2009; Shen et al., 2019) in a plane oriented perpendicular to the propagation direction. OAM has an infinite number of modes and each mode is orthogonal to the others (Beijersbergen et al., 1993; Rogel-Salazar et al., 2014; Xie et al., 2017b). As early as 1959, Richards et al. (Richards and Wolf, 1959) analyzed the energy flow near an abnormal halo at the focal plane of a lens. In 1967, Boivin et al. (1967) discovered that a vortex is present in the energy flow that revolves around a line located near the focal plane. In 1974, Nye and Berry (1974) proved that the existence of phase defects causes the optical vortices, which then led to the development of phase singularities in optical fields. In 1985, Kruglov and Vlasov studied the space vortex soliton (Kruglov and Vlasov, 1985). When the nonlinear effect produced by a nonlinear medium interacts with the diffraction of light, dislocation of the spiral will produce a self-trapped vortex beam, i.e. the space vortex soliton. The vortex beam's phase features a spiral structure with a singularity at its center (Kivshar and Ostrovskaya, 2001).

In 1989, Coullet et al. (1989) found that the singularity in the laser cavity at the location where the electric field intensity is zero can exist for long periods in an unstable field that is higher than the threshold voltage. At the same time, the phase around this singularity changes constantly. They also discovered the vortex solution to the Maxwell-Bloch equation and created the concept of optical vortices after taking inspiration from the fluid mechanics vortex. In 1992, Allen et al. (1992) reported that one type of light carries a spiral phase $exp(il\varphi)$ corresponding to the OAM of light. Here, φ is the azimuthal coordinate, l is the topological charge, and each photon carries an OAM of $l\hbar$. One particularly useful OAM-carrying beam is Laguerre-Gaussian (LG) beam. Since then, the OAM-carrying beams have been widely investigated in optical manipulations (Grier, 2003; Zhuang, 2004), optical communications (Barreiro et al., 2008; Wang et al., 2012; Bozinovic et al., 2013), precision measurement (Cvijetic et al., 2015; Kravets et al., 2013), astronomy (Lee et al., 2006; Tamburini et al., 2011), optical imaging (Fürhapter et al., 2005; Tamburini et al., 2006), optical multiplexing holography (Fang et al., 2021; Fang et al., 2020), laser (Zhang et al., 2020; Wei et al., 2019a; Naidoo et al., 2016; Sroor et al., 2020), nonlinear and quantum optics (Wei et al., 2017; Chen et al., 2020; Wei et al., 2019b; Zhou et al., 2014c; Zhou et al., 2014b). Interestingly, the vortex wavefront of the OAM beam can be used to perform rotation

* Corresponding author.
E-mail address: zhangyong@nju.edu.cn (Y. Zhang).
[1] These authors contribute equally to this work.

https://doi.org/10.1016/j.rio.2021.100158
Received 7 August 2021; Received in revised form 26 September 2021; Accepted 30 September 2021
Available online 5 October 2021

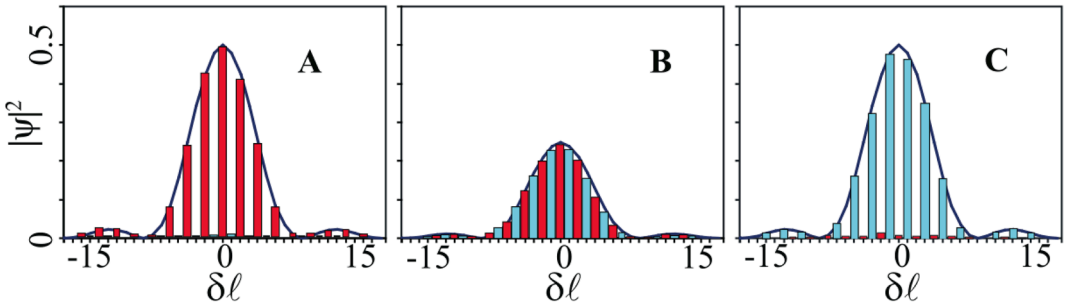

Fig. 1. Panels A, B and C show the observed angular momentum spectra for $\delta\Phi = 0$, $\pi/2$ and π for two equi-spaced segment apertures of angular width $2\pi/9$, respectively (Yao et al., 2006). Reproduced from (Jack et al., 2008) with permission.

measurements (Lavery et al., 2013). Zhang et al. demonstrated low-photon static weak rotation measurements by the geometric phase distribution of the OAM light beam (Zhang et al., 2016). In this review, we focus on the applications of OAM in rotation measurements including object orientation recognition, rotation sensing, small angle measurement, and rotating object imaging.

1.2. OAM mode decomposition: Fourier relation of angular position and OAM

As a physical quantity connected with the azimuthal information of optical fields, the OAM can be related to the angular position via a Fourier relationship, in a manner similar to linear momentum and linear position (O'Neil et al., 2002; Franke-Arnold et al., 2004; Yao et al., 2006). Considering the 2π periodic nature of the angular variable, the relationship is a Fourier series leading to discrete values for the angular momentum, which can be expressed as (Yao et al., 2006).

$$\psi_l = \frac{1}{\sqrt{2\pi}}\int_{-\pi}^{+\pi} d\phi\Psi(\phi)exp(-il\phi), \tag{1}$$

$$\Psi(\phi) = \frac{1}{\sqrt{2\pi}}\sum_{l=-\infty}^{+\infty}\psi_l exp(il\phi), \tag{2}$$

where ψ_l represents the OAM distribution and $\Psi(\phi)$ is the angular distribution. Eq. (2) indicates that an arbitrary angular distribution can be regarded as a coherent combination of the different OAM modes.

To verify this theory, one can analyze the OAM spectra of different angular distributions. When a pure OAM state represented by $exp(il\phi)$ is incident into an aperture or a mask $\Psi_{Mask}(\phi)$ with an angular dependence, the transmitted field is then written as

$$\Psi_{Transmitted}(\phi) = exp(il\phi)\times\Psi_{Mask}(\phi). \tag{3}$$

According to Eq. (2), the transmitted field can be expressed in terms of its angular harmonics using the Fourier coefficients A_n, i.e.,

$$\Psi_{Transmitted}(\phi) = \sum_{n=-\infty}^{+\infty} A_n exp(i(l+n)\phi), \tag{4}$$

where $\sum_{n=-\infty}^{+\infty}|A_n|^2$ is the total intensity transmission of the mask. From Eq. (4), the OAM component of the incident light acquires OAM sidebands that are shifted by $\delta l = n$ and their amplitudes are given by the corresponding Fourier coefficient of the mask. An example of angular masks is analyzed here to demonstrate the modifications to the incident OAM components. A single-segment mask with a hard-edged aperture segment with a width of Θ,$\Psi_{Mask}(\phi) = 1$ for $-\Theta/2 < \phi < \Theta/2$ and 0 elsewhere, i.e.

$$\Psi_{Mask}\left(\frac{\phi}{\Theta}\right) = \begin{cases} 1, & |\phi| \leqslant \frac{\Theta}{2} \\ 0, & \frac{\Theta}{2} < |\phi| \leqslant 2\pi \end{cases}. \tag{5}$$

The Fourier transform of the angular distribution of the mask is (Jack, 2011)

$$\mathrm{F}\left\{\Psi_{\mathrm{Mask}}\left(\frac{\phi}{\Theta}\right)\right\} = \frac{sin\pi\mathrm{n}\Theta}{\pi\mathrm{n}} = \Theta sinc(\mathrm{n}\Theta). \tag{6}$$

So the mask can be decomposed into different OAM components as follows

$$\Psi_{Mask}(\phi) = \frac{\Theta}{2\pi}\sum_{n=-\infty}^{+\infty}\mathrm{sinc}\left(\frac{n\Theta}{2}\right)exp(in\phi). \tag{7}$$

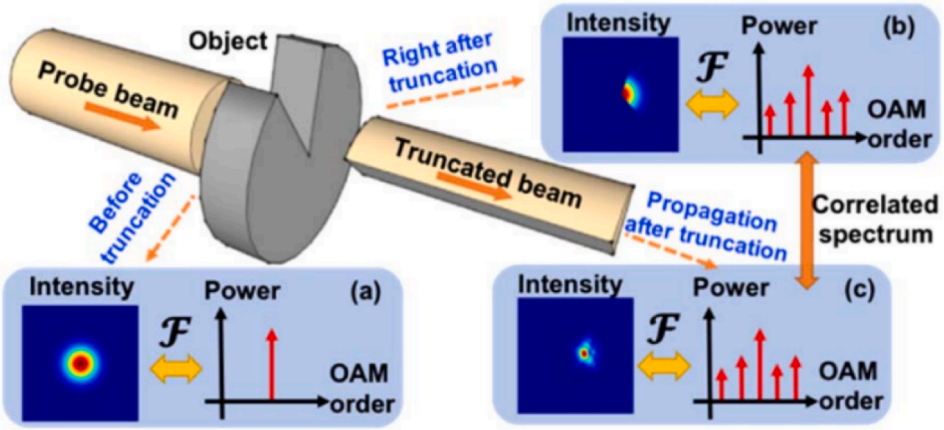

Fig. 2. Schematic of using the OAM spectrum to measure an object's parameters. The beam's intensity profile and OAM spectrum (a) before object truncation, (b) right after object truncation, and (c) certain distance after object truncation (Xie et al., 2017b). Reproduced from (Jack et al., 2008) with permission.

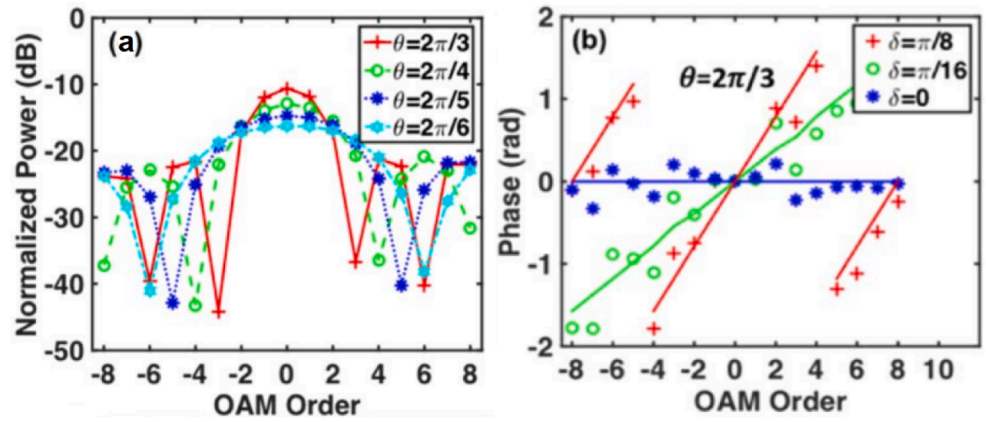

Fig. 3. (a) The OAM intensity spectra measured for the light truncated by objects having various opening angles θ. (b) OAM phase spectra measured for the light truncated by an object having an opening angle of $2\pi/3$ but various orientation angles δ (Xie et al., 2017b). Reproduced from (Jack et al., 2008) with permission.

The incident OAM beam will thus be modified and shifted by an envelope composed of a *sinc* function. When a mask with *m*-fold rotational symmetry that comprises *m* identical equally-spaced apertures, i.e.,

$$\Psi_{Mask}^{(m)}(\varphi) = \sum_{q=1}^{m} \Psi_{Mask}\left(\phi + q\frac{2\pi}{m}\right), \tag{8}$$

The corresponding modification function is

$$\psi_{\delta l}^{(m)} = A_{\delta l} \sum_{q=1}^{m} exp\left(i\frac{q}{m}2\pi\delta l\right) = \begin{cases} mA_{\delta l} & for \quad \delta l = Nm \\ 0 & otherwise \end{cases}, \tag{9}$$

where N is an integer. Therefore, for an *m*-fold rotational symmetry mask, only every m^{th} sideband with the *sinc* envelope will be present (see Fig. 1A). Considering more complex situations where each of the *m* hard-edged aperture segments has a definite and non-zero relative phase $\delta\Phi$, the modification function of each OAM component can be regarded as the interference caused by the modulation of every aperture (see Fig. 1B and C).

In 2008, Jack et al. concluded that the Fourier relationship between OAM and angular position is that of an angular diffraction, i.e., a mask that blocks light within one or several angular apertures represents the angular analogue of a single slit or a diffraction grating, respectively (Jack et al., 2008).

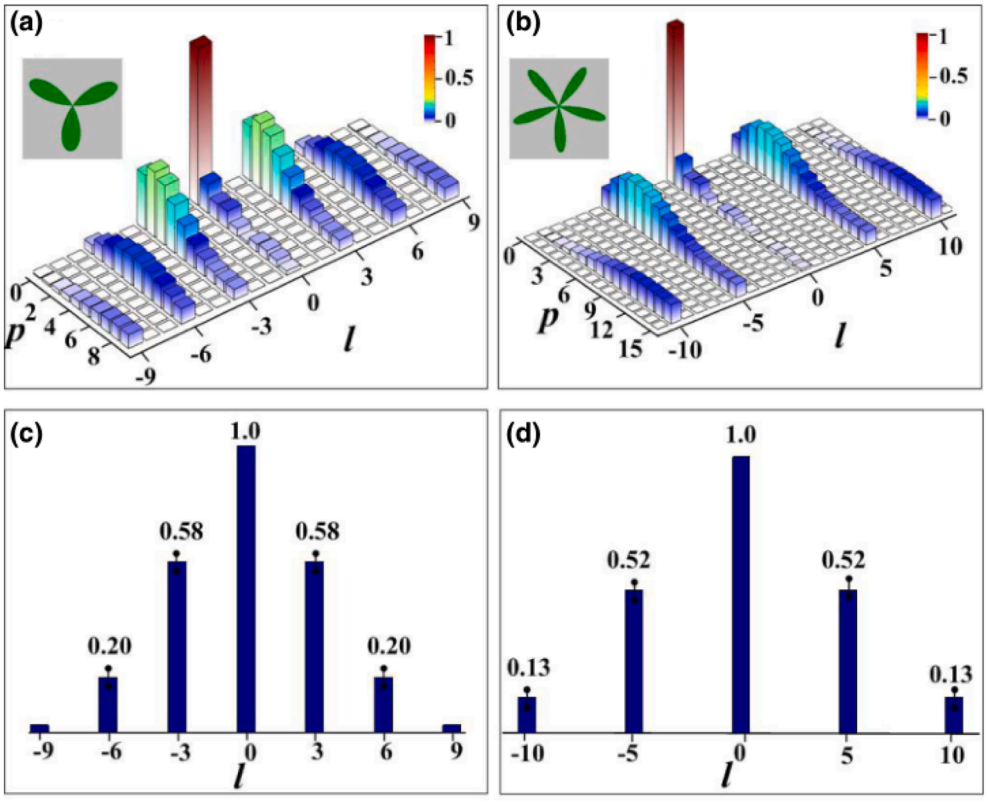

Fig. 4. Schematic of the spiral spectra of the symmetrical objects. The top panels are the peak-normalized laguerre-gaussian mode spectra while the bottom panels are the OAM spectra. (a), (c) A three-leaf clover. (b), (d) A five-petal pentas (Zhang et al., 2018). Reproduced from (Jack et al., 2008) with permission.

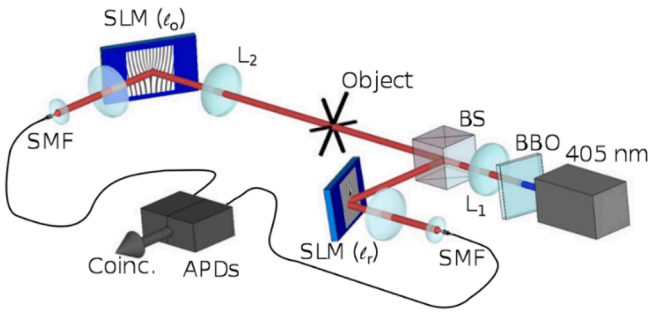

Fig. 5. Scheme of the experiment setup for the sensing of the object via orbital angular momentum of correlated photons (Uribe-Patarroyo et al., 2013). Reproduced from (Jack et al., 2008) with permission.

2. Optical field analysis based on the OAM spectrum

2.1. Azimuthal identification of objects

Based on the Fourier relationship between the OAM and the angular position, several sensing techniques to detect an object's azimuthal information have been proposed. By analyzing the OAM spectrum of the optical field after it passes through the target object, the target's azimuthal structure can be acquired clearly (Fitzpatrick et al., 2014). An object-truncated Gaussian beam can be decomposed into a set of OAM-carrying modes (see Fig. 2(a) and (b)) (Xie et al., 2017b).

The distribution of the complex OAM spectrum is related to the parameters of the object. For example, the dip positions of the OAM intensity spectrum are dependent on the object's opening angle θ and the slope of the OAM phase spectrum is decided by the opening's orientation δ. If the topological number of the incident OAM is l_1, the measured OAM component of l_2 vanishes when $l_1 - l_2 = 2\pi N/\theta$ (see Fig. 3(a) with $l_1 = 0$). When the object's orientation angle is δ, the slope of the measured phase is also approximately δ, as shown in Fig. 3(b).

Additionally, one can deduct from Eq. (9) that the OAM spectrum reflects the rotational symmetry of an object. Fig. 4 shows a three-leaf clover and a five-leaf clover along with their corresponding OAM spectra. Only the OAM components with indices that are multiples of three or five exist. Based on this characteristic, the rotational symmetry of an object can be identified clearly using its OAM spectrum (Zhang et al., 2018).

OAM-based sensing techniques can also be used in ghost imaging (Uribe-Patarroyo et al., 2013; Simon and Sergienko, 2012). As shown in Fig. 5, when spontaneous parametric down-conversion (SPDC) is used as a source of correlated photon pairs, the resulting two-photon joint OAM spectrum can provide information about the spatial symmetries for efficient object recognition.

More interestingly, the Hanbury Brown and Twiss (HBT) interferometry technique with twisted light (Magaña-Loaiza et al., 2016) reveals the intensity correlations among the OAM components and the angular positions of pseudothermal light (Fig. 6). The technique is capable to identify the spatial signatures and phase information of an object with rotational symmetries by using random light. This method is robust against environmental noise and thus demonstrates promising potential for remote sensing in realistic schemes.

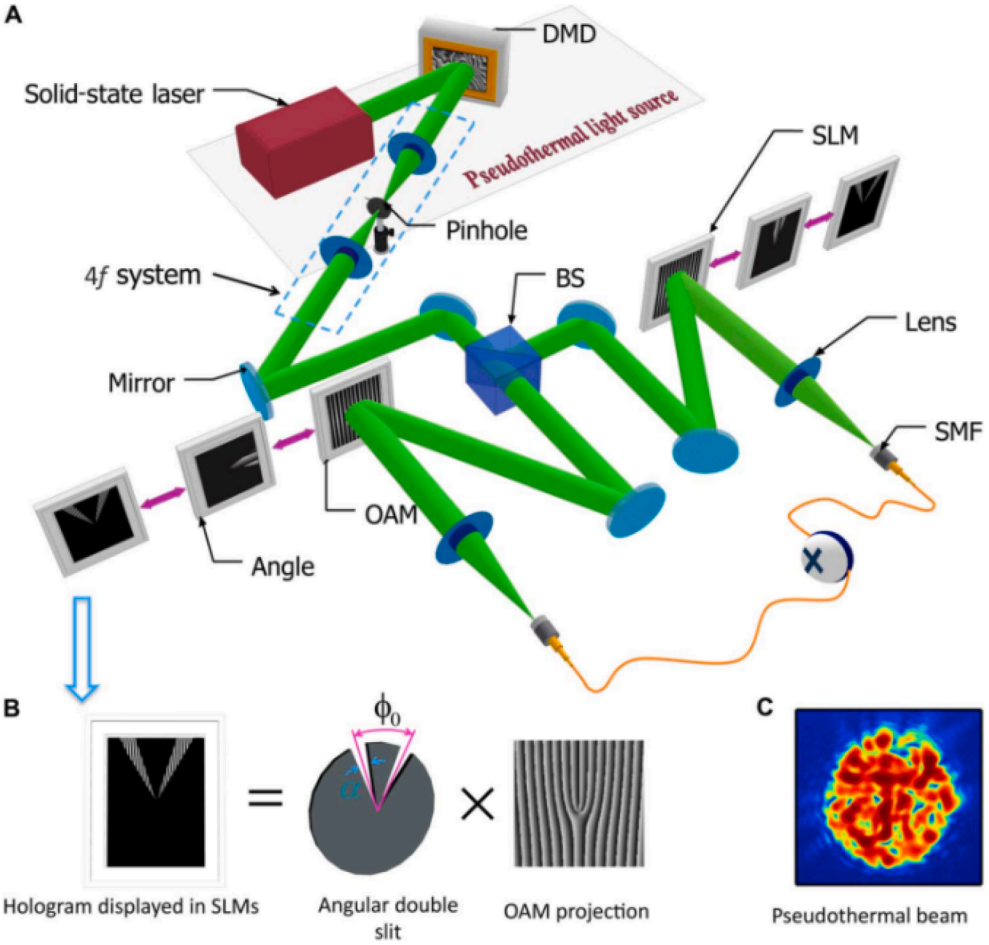

Fig. 6. (A) Scheme of the experiment setup for the study of the azimuthal HBT effect. (B) For the HBT measurements, a pair of angular slits is encoded onto the SLMs. (C) Intensity distribution of a generated pseudothermal beam of light (Magaña-Loaiza et al., 2016). Reproduced from (Jack et al., 2008) with permission.

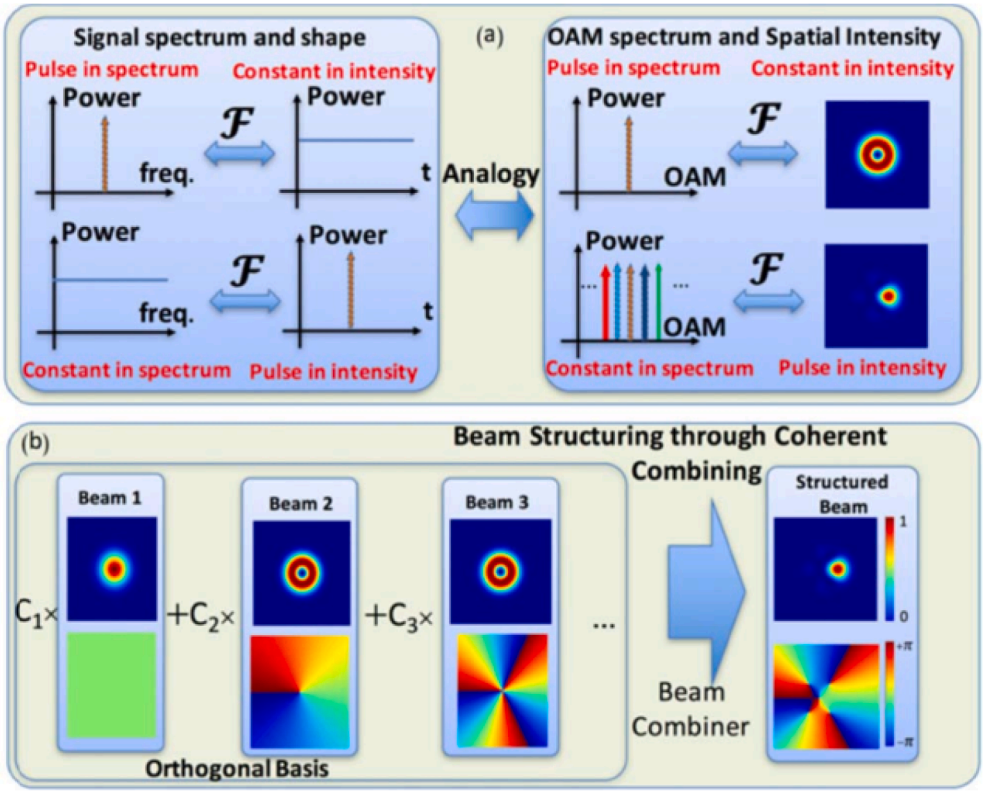

Fig. 7. (a) Schematic of analogy between the "frequency-time" relationship of a signal and the "OAM spectrum-spatial intensity" relationship of a beam. (b) Beam structuring through coherently combining several beams from an orthogonal modal basis with complex coefficients C_i (Xie et al., 2017a). Reproduced from (Jack et al., 2008) with permission

2.2. Digital spiral imaging

In 2005, Torner and Torres proposed the concept of digital spiral imaging (DSI) (Torner et al., 2005; Molina-Terriza et al., 2007), in which the OAM spectrum of a light beam is used to image canonical geometrical objects. This work opens the door to OAM-based imaging (Chen et al., 2014). Proper selection of a weighted combination of multiple modal states within an orthogonal OAM basis set will allow any desired azimuthal beam intensity profile to be created (Xie et al., 2017a) (Fig. 7). In addition, by imparting an extra phase factor into each constituent OAM mode, it is easy to realize the rotation and reflection of an image (Li et al., 2018).

2.3. Laguerre-Gaussian mode-based imaging

OAM mode has unique advantages for azimuthal sensing and imaging. However, because of the lack of radial components, it is not sufficient to construct a two-dimensional optical field alone. Therefore, attention has been paid to one special OAM-carrying mode, i.e., LG mode, which is capable to characterize the radial information via its p index.

Several methods (D'Errico et al., 2017; Xiao et al., 2019) have been proposed to decompose an optical field into its LG modes for optical image processing. Xiao et al. used a subspace projection method to achieve LG mode expansion of arbitrary optical fields. They defined a space-bandwidth product and proposed several criteria to determine the parameters of the used LG modes including the beam waist and the truncation order. Generally, the beam waists determined using this method are different in each OAM subspace. Recently, Ma et al. proposed a systematic scheme to determine the parameters for efficient LG mode expansion, in which an optimized beam waist is utilized for all LG components (Ma et al., 2021). Also, they demonstrated azimuthal noise

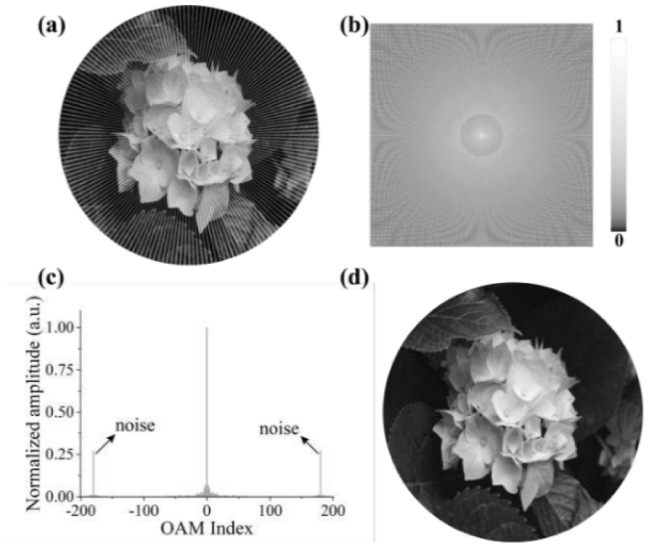

Fig. 8. Results of image noise filtering. (a) Raw image with azimuthal noise recorded by a linear array CCD. (b) The corresponding Fourier spectrum. (c) The corresponding l spectrum. (d) The reconstructed image after LG domain filtering (Ma et al., 2021). Reproduced from (Jack et al., 2008) with permission

filtering based on the LG modes (as shown in Fig. 8), which presents the unique advantage of using LG modes in polar image processing. By manipulating the LG spectrum, image edge enhancement, image rotation, image replication and noise filtering can easily be realized.

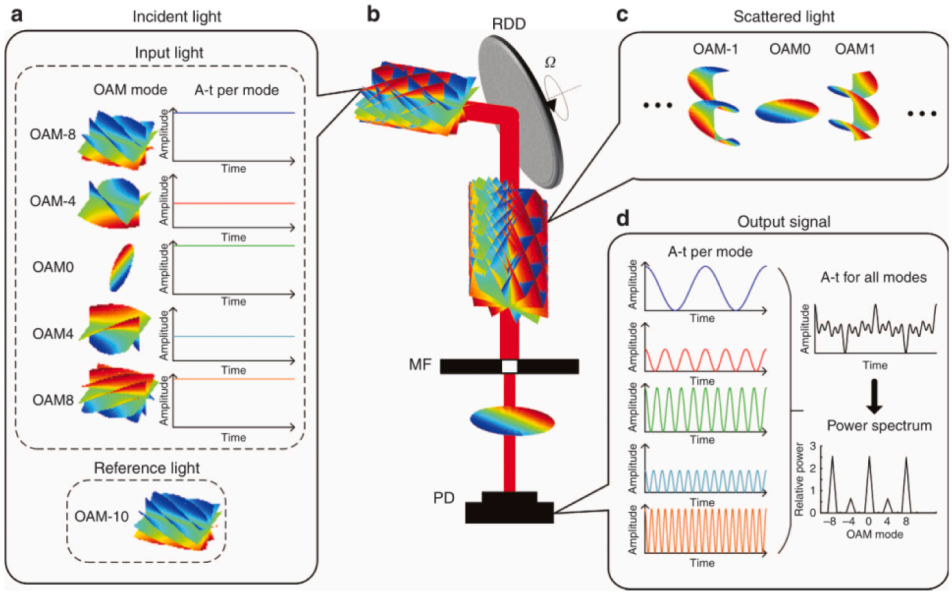

Fig. 9. (a) The incident light is composed of the input light and a reference light. (b) Schematic of the OAM complex spectrum analyzer. (c) The scattered light is composed of numerous OAM modes. (d) The output signals are received by the photodetector. The beat frequency varies linearly with respect to the topological charge of the input mode, and the amplitude is proportional to that of the input mode. The power spectrum can be obtained through a Fourier transform of the total intensity (Zhou et al., 2017). Reproduced from (Jack et al., 2008) with permission

3. Detection of rotating objects based on OAM spectrum measurement

3.1. Rotational Doppler effect

The linear Doppler effect is a well-known phenomenon. When a relative movement occurs between an emitter and an observer, there will be a difference between the frequency received by the observer and the original frequency of the wave source. The linear Doppler effect has been extensively investigated for its applications in radar, Doppler velocimetry, laser interferometers, and so on. In recent years, the research development in OAM beams has led to the discovery of

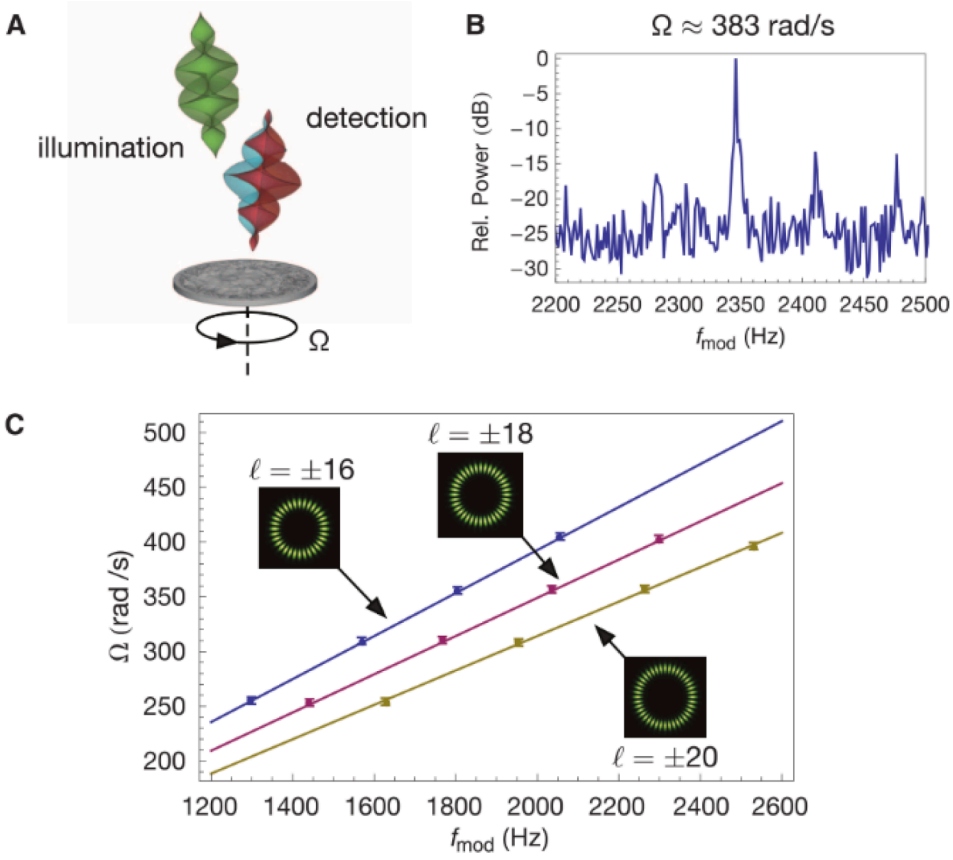

Fig. 10. (A) A superposition of helically phased beams with opposite signs of l, incident on a surface rotating at a speed Ω. (B) The intensity modulation at a particular frequency result from the differential shift, $f_{mod} = 2346 \pm 1$. (C) Values of f_{mod} were measured for different rotation speeds and values of $|l|$ (Lavery et al., 2013). Reproduced from (Jack et al., 2008) with permission.

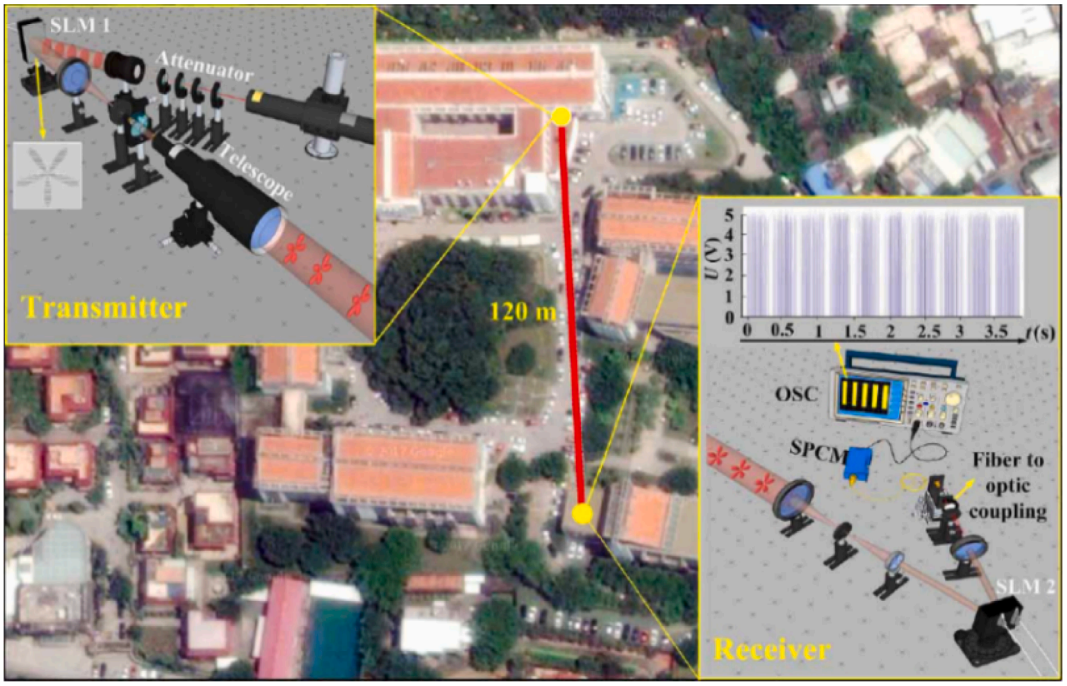

Fig. 11. 120-m free-space optical link implemented from building-to-building in the Haiyun Campus of Xiamen University (Zhang et al., 2018). Reproduced from (Jack et al., 2008) with permission.

rotational Doppler effect (Bialynicki-Birula and Bialynicka-Birula, 1997; Courtial et al., 1998a; Fang et al., 2017).

In the 1970s, Garetz (Garetz and Arnold, 1979; Garetz, 1981) reported that for circularly polarized light, rotational motion between the source and the observer causes a frequency shift of $\Delta\omega = \pm\sigma\omega$. Here, ω is the angular velocity and $\sigma = \pm 1$ for the right-hand-polarized and left-hand-polarized light beams, respectively. In 1994, Allen predicted (Allen et al., 1994) that an atom moving in a light beam with orbital angular momentum experiences an azimuthal shift in the resonant frequency in addition to the usual axial Doppler and recoil shifts when a beam of light is incident on the surface of a rotating object. Therefore, the frequency of the object's rotation can be determined by measuring the OAM. In 1998, Courtial et al. proved that rotation of a beam causes a frequency shift related to the total angular momentum of the beam (Courtial et al., 1998a; Courtial et al., 1998b). This effect is called the rotational Doppler shift (Basistiy et al., 2002; Barreiro et al., 2006). When an OAM light beam with a topological number l illuminates a spinning object with a rotation speed Ω and the topological number of the scattered light is m, the rotational Doppler shift is then given by

$$\Delta f = (l - m)\Omega/2\pi \tag{10}$$

An OAM complex spectrum analyzer based on the rotational Doppler effect has been developed. It can measure the power and phase distributions of the OAM components simultaneously. The technique used in this analyzer is illustrated in the diagram shown in Fig. 9 (Zhou et al., 2017).

Along with a high-power reference light beam, a light beam containing different OAM components is incident onto a spinning object. The scattered light passes through a mode filter to select the zero-order OAM mode. The alternating current (AC) intensity of the energy collected by a photodetector can be expressed approximately as:

$$I_{m,AC}(\gamma) \approx 2\gamma \sum_{1 \leqslant p \leqslant N} \left| B_p A_{m-l_p} B_0 A_{m-l_0} \right| cos\left[\left(l_p - l_0 \right) \Omega t + \phi_{p,0} \right] \tag{11}$$

where B_p is the complex amplitude of the OAM mode, A_{m-l_p} is the Fourier expansion coefficient of the spinning object. B_0 and A_{m-l_0} describe the reference light beam. If all the coefficients are known, the OAM spectrum can be obtained by performing a Fourier transform on the intensity collected by the photodetector. This method has potential applications in spatial mode analysis and mode-division multiplexing optical communication.

3.2. Rotational speed measurement

One important application of rotational Doppler effect is the measurement of the velocity of a spinning object. When a spinning object is illuminated by two OAM beams with opposite values of l, the frequency of the scattered light will be blue-shifted and red-shifted for the positive and negative l respectively (see Fig. 10A) (Lavery et al., 2013). Then the intensity modulation caused by the opposite frequency shift is given by

$$f_{mod} = \frac{2|l|\Omega}{2\pi} \tag{12}$$

An example is presented in Fig. 10B. The rotating surface is illuminated by using OAM beams of $l = \pm 18$. The calculated differential frequency is $f_{mod} = 2346 \pm 1$ Hz and the rotational speed is 383 rad/s. Fig. 10C shows the results when changing the rotation speed and the value of $|l|$, illustrating a further test of the relationship predicted in Eq. (12).

To satisfy the requirements of practical inspection environments, additional improvements based on the rotational Doppler effect have been developed (Cvijetic et al., 2015; Zhang and Ma, 2017). For example, Zhai et al. proposed a time–frequency analysis method to estimate the angular acceleration of a spinning object through short-time Fourier transform (STFT) (Zhai et al., 2019). Qiu et al. analyzed the effect of lateral misalignment of the incident light and showed a broadened frequency shift around the center frequency (Qiu et al., 2019a). Qiu et al. also investigated the rotational Doppler effect at oblique incidence based on a local scattering model. They formulated a quantitative relationship between the Doppler frequency shift and the tilt angle (Qiu et al., 2019b).

Notably, the OAM-based measurement of rotational speed is mainly limited by the response speed of the detector and the available high-order OAM mode. In comparison to the traditional methods, OAM-

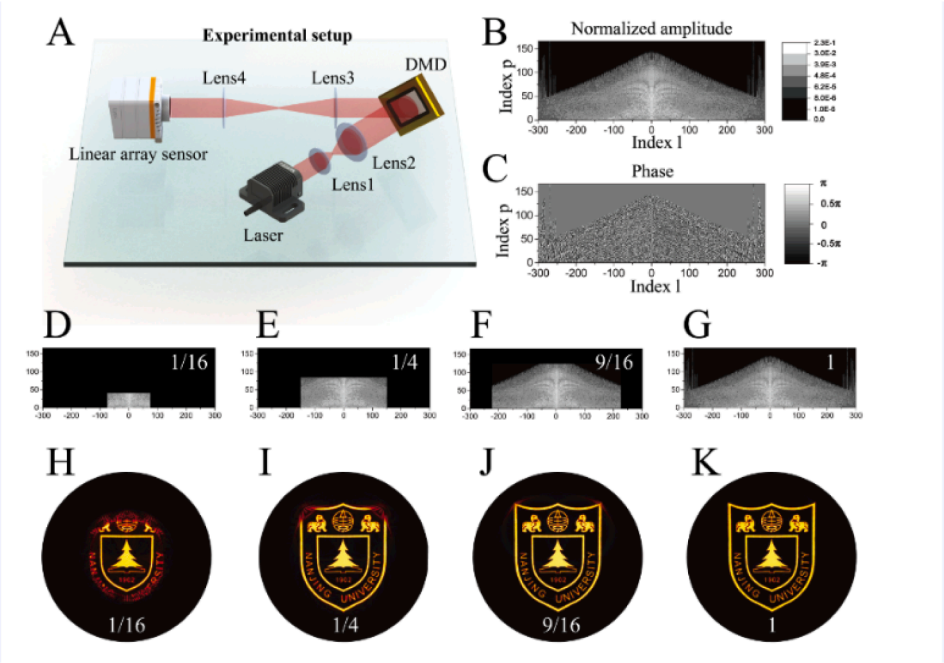

Fig. 12. (A) Scheme of the experiment setup for a series of amplitude patterns are playing on the DMD to mimic a rotating object. (B) and (C) are the amplitude and phase of the measured LG spectrum from a rotating emblem of Nanjing University. (D)–(G) show used portions of the LG spectrum to reconstruct the emblems displayed in (H)–(K), respectively (Wei et al., 2020). Reproduced from (Jack et al., 2008) with permission.

based method provides a non-contact way to precisely measure the rotational speed.

3.2.1. Rotating object imaging techniques

As we discussed in Section 2.2, it is possible to determine azimuthal structures of an object by reading the shape of the OAM spectrum. Similarly, by measuring the OAM spectrum of a spinning object, one can also acquire its azimuthal information. As shown in Fig. 11, Zhang et al. established a 120-m-long free-space link between the rooftops of two buildings. Both the rotational speed and the rotational symmetry of an object were obtained from the rotational-Doppler-frequency-shifted signal at low photon-count level (Zhang et al., 2018). Because of the use of OAM, this method is robust and feasible for use in practical environment such as atmospheric turbulence.

In many practical applications, it is important to recover the entire 2D structures of rapidly rotating objects. Wei et al. proposed an LG transform for rotating image processing (Wei et al., 2020). Based on rotational Doppler effect and radial mode fitting, they measured the complete LG spectrum of the rotating object. Interestingly, the LG spectrum remains unchanged during the object's rotation. They experimentally performed typical image processing operations such as image reconstruction, edge enhancement and pattern replication (Fig. 12). This method demonstrates the unique advantages of rotational object imaging based on LG modes.

4. Detection of angular movement based on an OAM-mode interferometer

4.1. Basic principle

In the early research on vortex beams, the interference patterns between screw-dislocation wave which has a wave front consisting of one helicoid or several helicoids and plane wave were investigated (Basistiy et al., 1993). The OAM mode's phase distribution contains a total of l cycles, where l is the topological charge. If the light spot with the OAM is rotated by a specific angle, the transverse phase distribution of the light spot will also be rotated by the same angle. Usually, an OAM beam can

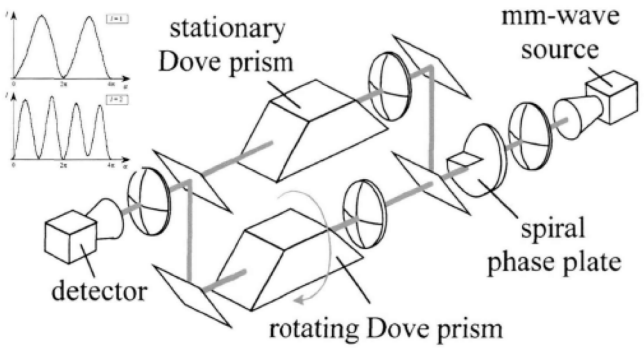

Fig. 13. The rotating measurement experiment using Dove prisms (Courtial et al., 1998a). Reproduced from (Jack et al., 2008) with permission.

be rotated by rotating a Dove prism. As early as 1988, Padgett (Courtial et al., 1998a) used a combination of a Dove prism and a Mach-Zehnder interferometer to measure rotation angles, as shown in Fig. 13. When the OAM beam passes through the Dove prism, it flips up and down; more importantly, when the Dove prism rotates by an angle of α, the OAM

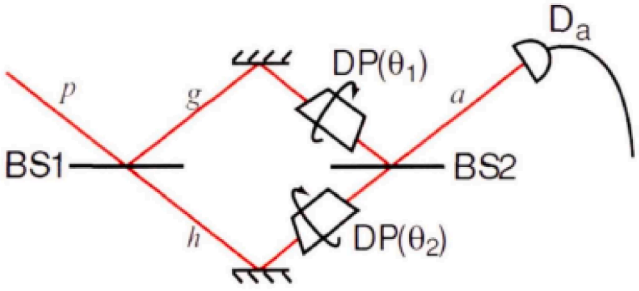

Fig. 14. Measurement of rotation angle by interferometer based on Dove prism (Jha et al., 2011). Reproduced from (Jack et al., 2008) with permission

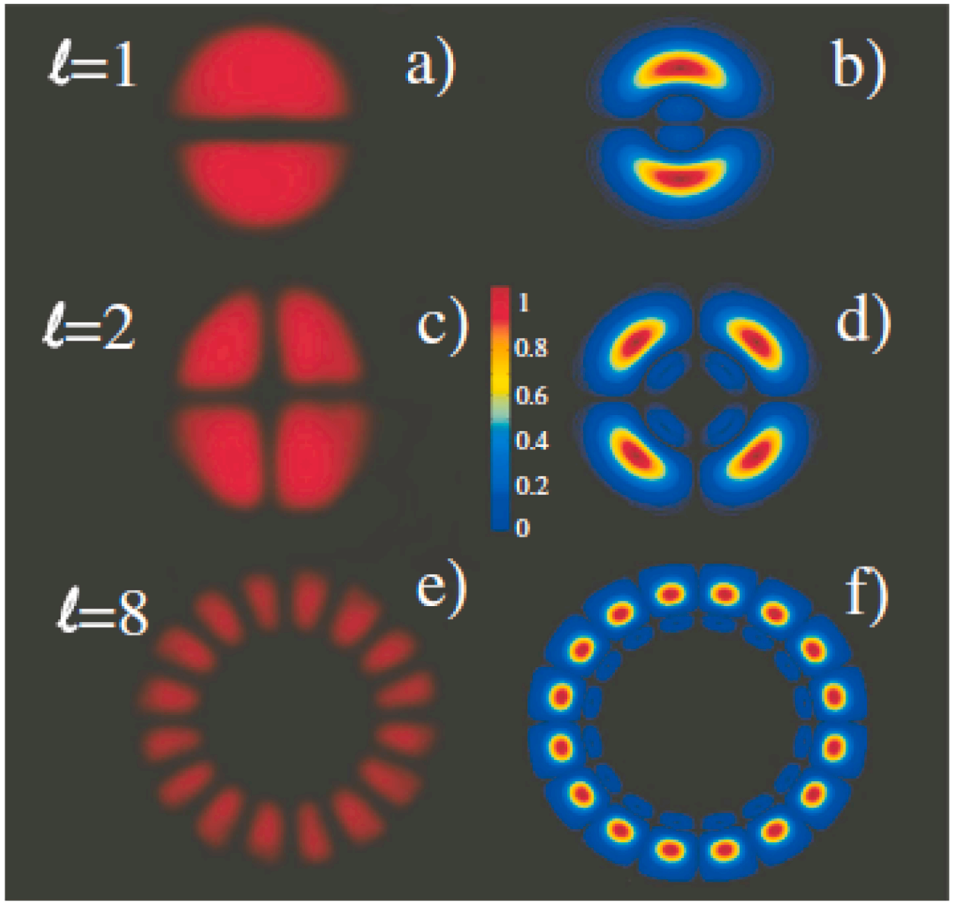

Fig. 15. Conjugate superimposed petal pattern of different l (Emile and Emile, 2017). Reproduced from (Jack et al., 2008) with permission.

beam will then rotate by an angle of 2α. One Dove prism is fixed and the other one is rotated.

In experiments, it is difficult to separate the frequency shift caused by the rotation from small experimental deviations (Basistiy et al., 2003). Therefore, interferometry methods are used to eliminate the experimental deviations from the optical path. For example, Jha et al. (2011) determined the angular displacement measurement sensitivity of an interferometer using a Dove prism (see Fig. 14).

The rotational angles of the two paths of the interferometer are θ_1 and θ_2. Assume that $|1_j\rangle_{a_{+l}}$ is the state of the jth photon in input mode a, including the mode index l of the OAM. The output state of the jth photon in mode a is then given by

$$|\phi_j\rangle = \frac{1}{2}\left(e^{-2il\theta_1} + e^{-2il\theta_2}\right)|1_j\rangle_{a_{+l}} \tag{13}$$

The total photon state at the output of the interferometer is given by:

$$|\psi\rangle = \prod_{j=1}^{N}|\phi_j\rangle = |\varphi\rangle e^{-i2l\Delta\theta} \tag{14}$$

Then, the expected count value for each photon with $l\hbar$ is $\left\langle \hat{N}_a \right\rangle = Ncos^2 l\theta$, where $\theta = \theta_1 - \theta_2$. The relevant uncertainty is $\left\langle \triangle \hat{N}_a \right\rangle^2 = \frac{N}{4} sin^2 l\theta$ and the signal to noise ratio of the relative angular displacement is given by

$$\frac{\left|\partial\left\langle \hat{N}_a \right\rangle/\partial\theta\right|}{\left\langle \triangle \hat{N}_a \right\rangle} = 2l\sqrt{N} \tag{15}$$

Compared with Courtial's work in Fig. 13, Jha et al. proposed a similar Mach-Zehnder interferometer except that both Dove prisms are rotated to eliminate the negative influence of misalignment to a certain extent (Fig. 14). The signal-to-noise ratio of this method is proportional to the OAM index l.

Generally, the interference pattern formed by the superposition of OAM light beams with $\pm\, l$ presents the shape of petals. The number of petals is twice the topological charge and the zero azimuth angle is dependent on the initial relative phase between the two arms of the interferometer. The petal pattern offers certain advantages when performing rotation angle measurements. In theory, the energy of each petal is uniform, and 2 l petals form a circle. For smaller angles, the actual rotation angle can be obtained by simply calculating the rotation angle of the pattern. In addition, according to formula (15), the signal to noise ratio of the measured angular displacement signal is proportional to OAM index l, which has unique advantages for the measurement of small angle.

For standard LG modes, the beam radius of the OAM beam at a specific position z is

$$w(z) = w_0\sqrt{1 + z^2/z_R^2} \tag{16}$$

At the Rayleigh length position of $z_R = \pi w_0^2/\lambda$, the electrical field of the OAM beam can be written as

$$E_l(r,\theta) = R_l(r)e^{il\theta} \tag{17}$$

Here, $R_l(r)$ is the amplitude distribution which dependents on the radial field strength and l (Guo et al., 2016). The field obtained from the interferometer is given by

$$E_l(r,\theta) + E_{-l}(r,\theta) = 2R_l(r)e^{il\theta/2}cosl\theta \tag{18}$$

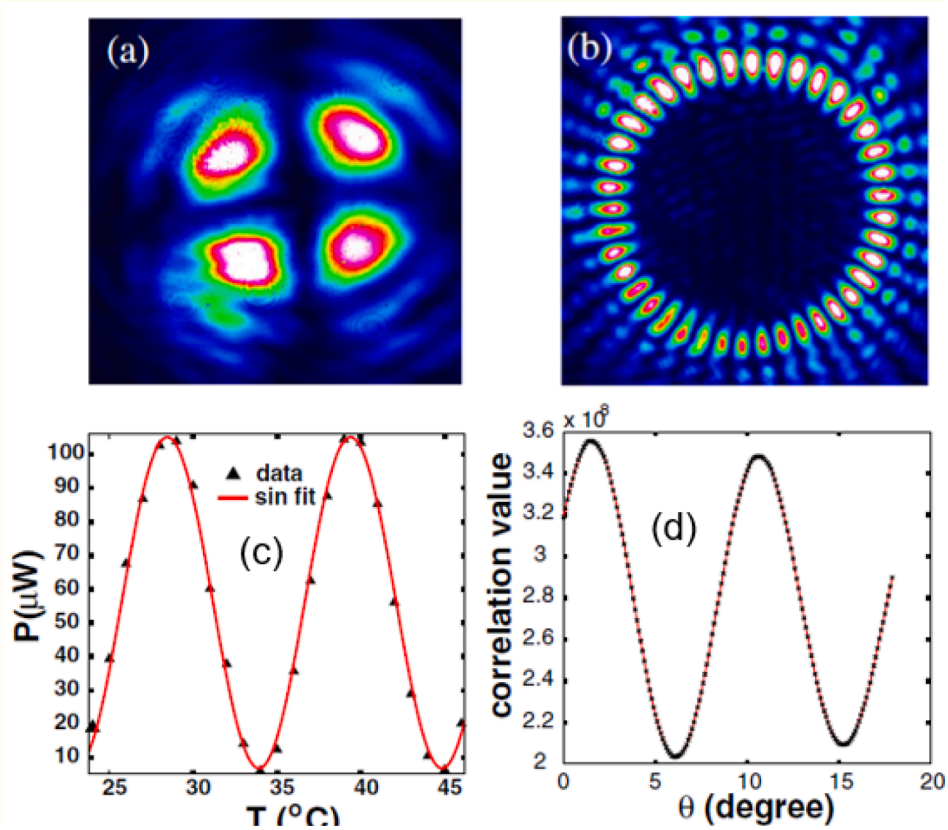

Fig. 16. (a) and (b) are the petal interference diagrams with $l = 2$ and 20 respectively; (c) The relationship between the leakage power of the hole and the crystal temperature when $l = 2$. (d) The angle change curve of the petal diagram with $l = 20$ (Zhou et al., 2014a). Reproduced from (Jack et al., 2008) with permission.

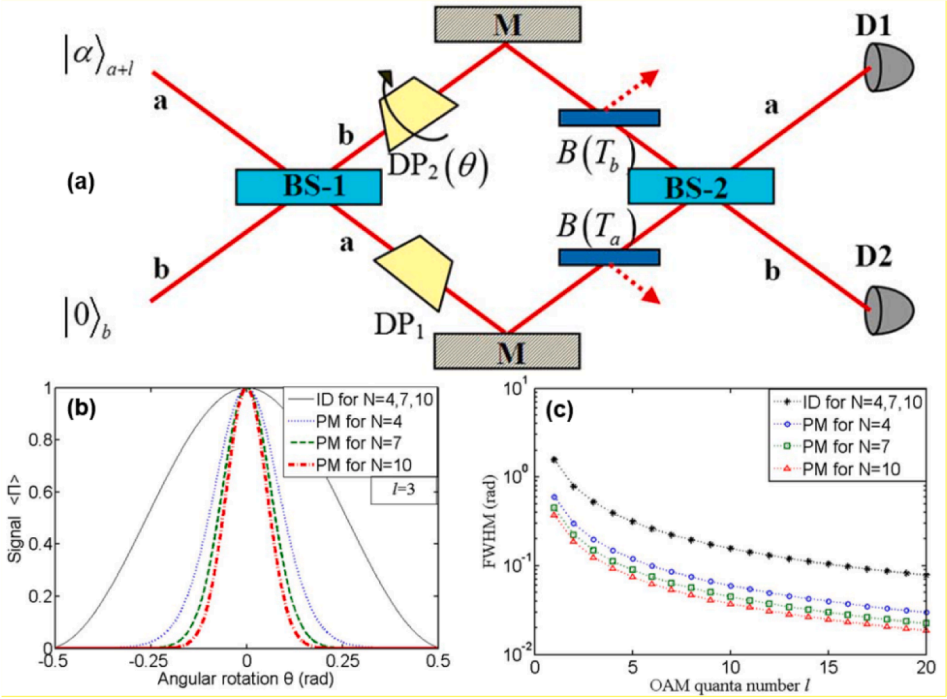

Fig. 17. (a) Scheme of the experiment setup for angular rotation parity measurement. (b) The relationship between the output signal of PM and ID method with various rotation angle. (c) The relationship between FWHM of PM and ID method and the used OAM quanta number l (Zhang et al., 2016). Reproduced from (Jack et al., 2008) with permission.

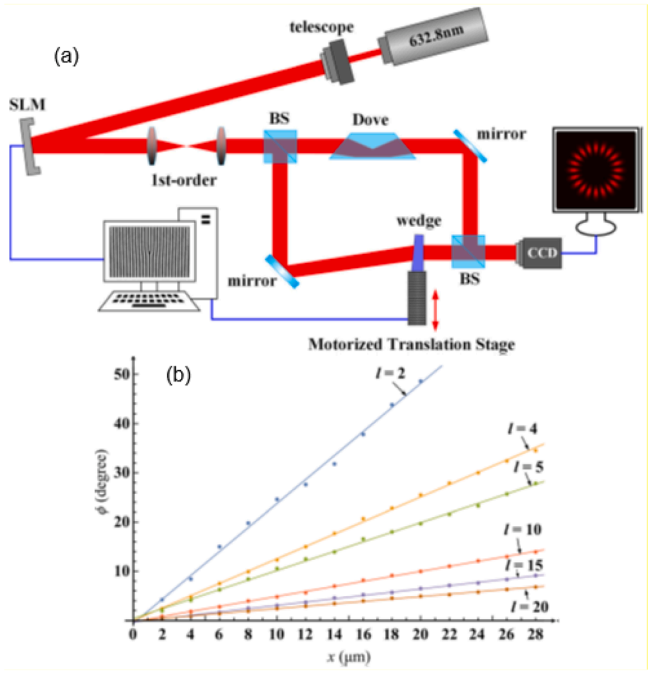

Fig. 18. (a) Improved Mach-Zehnder interferometer with Dove prism and optical wedge. (b) Schematic of the measurement results of the rotation angle of φ produced by wedge translation $\times$ for different petal patterns (Jia et al., 2017). Reproduced from (Jack et al., 2008) with permission.

The total light intensity is $I(r) = |2R_l(r)|^2 cos^2 l\theta$.

The field intensity of the petal pattern is angularly modulated. Fig. 15 shows the petal patterns with $l = 1$, 2 and 8. When the two arms of the interferometer produce a phase difference φ, the expression for the light field is given by Emile and Emile (2017):

$$E_l(r,\theta) + E_{-l}(r,\theta) = R_l(r)\left[e^{i(l\theta+2k\varphi)} + e^{-il\theta}\right] = 2R_l(r)e^{ik\varphi}cos(l\theta + k\varphi) \quad (19)$$

where $k = 2\pi/\lambda$. When the interferometer produce a phase difference φ, the spatial intensity distribution of the petal pattern will rotate by $2\pi\varphi/\lambda$. When the two arms of the interferometer do not produce a phase shift and the beam itself rotates by a specific angle of θ, the spatial intensity distribution of the petal pattern will then rotate by $l\theta$. By using a Michelson interferometer, Emile et al. measured the angular displacement through analyzing the phase change of the petal interference pattern (Fig. 15). Based on this theory, many applications of tiny angle measurement using OAM have been reported.

4.2. Rotation angle measurement

In 2013, D'Ambrosio et al. (2013) proposed the concept of photonic gear and demonstrated NOON-like photonic states composed of l quanta of angular momentum ranging up to $l = 100$. The angular rotation of each photon can be converted into the amplified rotation of the light polarization, which is enlarged by l times. When compared with previous measurement methods, the accuracy of this angular measurement method is improved by nearly two orders of magnitude. The photonic scheme proposed in this work has major advantages when used in diagonal measurement of the mixed polarization OAM quantum state.

The weak value amplification of the angular signal is another important approach. In 2014, Magaña-Loaiza et al. (2014) used the shift of the OAM spectrum caused by polarization perturbation of the spin–orbit angular momentum coupling to measure the angular position. It is done by an amplification of both the real and imaginary parts of the weak-value of a polarization operator that has been coupled to the pointer. This method can enlarge small angles of rotation by up to 100 times.

In 2014, Zhou et al. (2014a) were able to rotate the interference pattern of a superimposed OAM beams with positive and negative l by adjusting the temperature and the electro-optic effect of a birefringent crystal, thus forming an optical rotator. When the optical path difference caused by the birefringent crystal is changed by 2π, the pattern is then rotated by an angle of π/l. The temperature and thermal-dispersion difference of the crystal can be determined through analysis of the rotating image. Fig. 16 shows an example with $l = 2$ and 20.

In 2016, Zhang et al. (2016) developed a parity measurement (PM) method for angular rotation measurement (Fig. 17(a)). When compared with the classical Malus law, the rotation angle measurement resolution is increased by l times. As shown in Fig. 17(b), the signal peak of the PM method is narrower than that of the early intensity detection (ID) method. As the number of photons increases, the signal peak of the PM result becomes narrower, which indicates a higher resolution. Fig. 17(c) shows that the full width at half maximum (FWHM) values of both the PM and ID methods decrease with the increase of OAM quanta number, and the FWHM of PM is always less than that of ID.

In 2017, Jia et al. (2017) proposed an improved Mach-Zehnder interferometer. A Dove prism was added to one arm and an optical wedge was inserted vertically into the other arm. The linear movement of the optical wedge could then equivalently cause rotation of the interference petal pattern. As shown in Fig. 18(a), the wedge moves vertically on the micrometer scale; its refractive index is n, the tilt angle is α, the wedge moves at a constant speed v, and the additional phase delay is $\theta = k(n-1)vttan\alpha$, where k is the wave vector. The interference petal pattern is given by Jia et al. (2017)

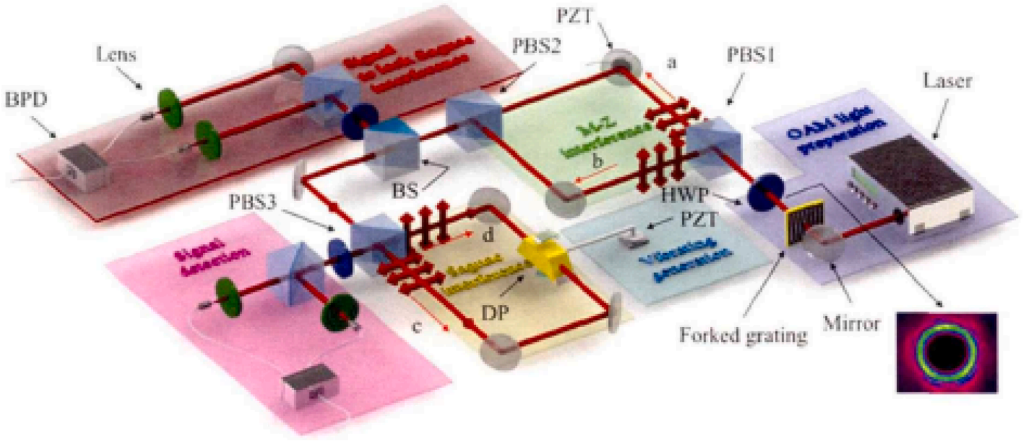

Fig. 19. Rotation angle measurement system in a Sagnac interferometer (Xiao et al., 2018). Reproduced from (Jack et al., 2008) with permission.

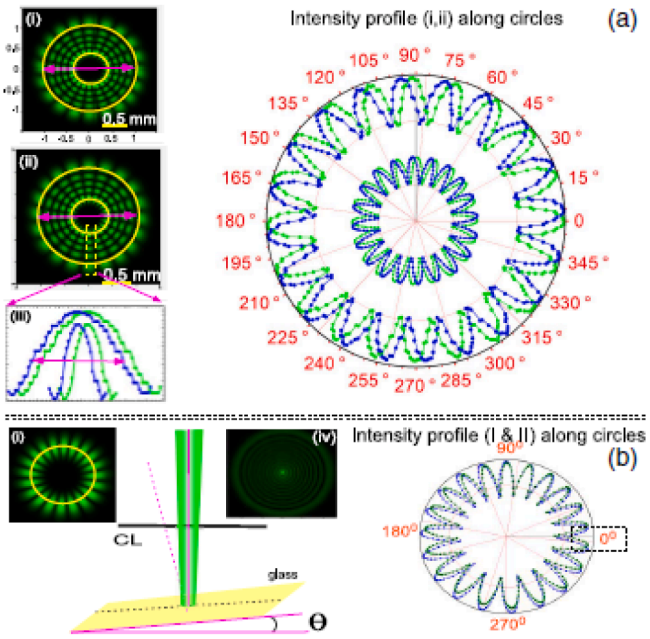

Fig. 20. (a) Petal interferogram with non-zero radial quantum number. (b) Tilt angle measured by using radial quantum number (Verma and Yadav, 2019). Reproduced from (Jack et al., 2008) with permission.

$$E(r,\theta) = E_l(r,\theta) + E_{-l}(r,\theta) \propto R_{lp}(r)\left[e^{-il(\theta+\Omega t)} + e^{il(\theta+\Omega t)}\right] \tag{20}$$

where $\Omega = \frac{\pi(n-1)tan\alpha}{\lambda l} v$. The recorded light intensity is expressed as

$$I(r,\theta) = 2|R(r)|^2(1 + cos[2l(\theta + \Omega t)]) \tag{21}$$

The optical wedge moves linearly at a speed v, which produces an equivalent rotational frequency shift of Ω. The measurement results are shown in Fig. 18(b), and the wedge translation step size is 2 μm. For different values of l, the rotation angle measurement results also tend to show linear behavior.

In 2018, Xiao et al. (2018) used two OAM beams incident in opposite directions on a Dove prism to form a Sagnac interferometer. As shown in Fig. 19, when the Dove prism rotates at an angle of θ, one of the beams will then produce a phase delay of $e^{2il\theta}$, while the beam incident in the opposite direction will produce a phase delay of $e^{-2il\theta}$. In this way, the signal can be doubled and the phase deviations of the different optical paths caused by the experimental system can also be eliminated. In the experiments, using an OAM beam with $l = 10$, the dynamic rotation angle at a vibration frequency of 650 Hz can be measured and the rotation angle resolution can reach approximately 1°.

Recently, attention has turned to the radial index p of the OAM (Karimi et al., 2014), which can enable finer fringes to be displayed in the interference pattern, thereby enhancing the sensitivity of the interferometer. In 2019, Verma and Yadav (2019) constructed interferometer using twisted light to detect picometer displacement. Through interference and superposition of two OAM light beams with opposite values of the topological charge l, they obtained a petal pattern. The relative displacements between the cylindrical lens and the solid and liquid surfaces can cause this petal pattern to rotate, and the angular displacement measurement resolution reached the picometer level. Fig. 20(a) shows the contours of the petal interference pattern with $l = 10$ before and after angular displacement. A minimum displacement of 3 pm could be measured using this technique. In addition, as shown in Fig. 20(b), the radial quantum number p can be used to measure the tilt angle of the surface. The interference pattern formed using the non-zero radial quantum number will show finer interference fringes that can be used to improve the rotation angle measurement accuracy.

5. Conclusions

Over the past 30 years, from the discovery of OAM to its widespread practical application, the developments made in OAM beams have been remarkable. The generation of a high-quality OAM beam is no longer a complex matter, which has promoted the application of OAM beams as a research hot spot in recent years. Because rotational motion is common in many practical industrial applications, the monitoring of objects with high rotational speeds or micro-scale rotation angles is critical. The abundant research in rotation sensing has demonstrated the advantages of OAM. In practical applications, it is necessary to provide further improvements in the accuracy and stability of OAM measurement systems. By further expanding on the theoretical research and breaking through the limitations of the current experimental conditions, OAM will be able to establish its importance in the precision measurement field in the near future.

Declaration of Competing Interest

The authors declare that they have no known competing financial interests or personal relationships that could have appeared to influence the work reported in this paper.

Acknowledgements

This work was supported by the National Key R&D Program of China (2017YFA0303703), the National Natural Science Foundation of China (NSFC) (91950206, 11874213, and 11904424), and Fundamental Research Funds for the Central Universities (021314380191 and 021314380105).

References

Allen, L., Babiker, M., Power, W.L., 1994. Azimuthal doppler-shift in light-beams with orbital angular-momentum. Opt. Commun. 112 (3-4), 141–144. https://doi.org/10.1016/0030-4018(94)00484-6.

Allen, L., Beijersbergen, M.W., Spreeuw, R.J.C., Woerdman, J.P., 1992. Orbital angular-momentum of light and the transformation of laguerre-gaussian laser modes. Phys. Rev. A 45 (11), 8185–8189. https://doi.org/10.1103/PhysRevA.45.8185.

Barreiro, J.T., Wei, T.-C., Kwiat, P.G., 2008. Beating the channel capacity limit for linear photonic superdense coding. Nat. Phys. 4 (4), 282–286. https://doi.org/10.1038/nphys919.

Barreiro, S., Tabosa, J.W.R., Failache, H., Lezama, A., 2006. Spectroscopic observation of the rotational doppler effect. Phys. Rev. Lett. 97 (11) https://doi.org/10.1103/PhysRevLett.97.113601.

Basistiy, I.V., Bazhenov, V.Y., Soskin, M.S., Vasnetsov, M.V., 1993. Optics of light-beams with screw dislocations. Opt. Commun. 103 (5-6), 422–428. https://doi.org/10.1016/0030-4018(93)90168-5.

Basistiy, I.V., Bekshaev, A.Y., Vasnetsov, M.V., Slyusar, V.V., Soskin, M.S., 2002. Observation of the rotational doppler effect for optical beams with helical wave front using spiral zone plate. JETP Lett. 76 (8), 486–489. https://doi.org/10.1134/1.1533771.

Basistiy, I.V., Slyusar, V.V., Soskin, M.S., Vasnetsov, M.V., Bekshaev, A.Y., 2003. Manifestation of the rotational doppler effect by use of an off-axis optical vortex beam. Opt. Lett. 28 (14), 1185. https://doi.org/10.1364/OL.28.001185.

Bazhenov, V.Y., Soskin, M.S., Vasnetsov, M.V., 1992. Screw dislocations in light wavefronts. J. Mod. Opt. 39 (5), 985–990. https://doi.org/10.1080/09500349214551011.

Beijersbergen, M.W., Allen, L., van der Veen, H.E.L.O., Woerdman, J.P., 1993. Astigmatic laser mode converters and transfer of orbital angular-momentum. Opt. Commun. 96 (1-3), 123–132. https://doi.org/10.1016/0030-4018(93)90535-D.

Bialynicki-Birula, I., Bialynicka-Birula, Z., 1997. Rotational frequency shift. Phys. Rev. Lett. 78 (13), 2539–2542. https://doi.org/10.1103/PhysRevLett.78.2539.

Boivin, A., Dow, J., Wolf, E., 1967. Energy flow in neighborhood of focus of coherent beam. J. Opt. Soc. Am. 57, 1171–2000. https://doi.org/10.1364/josa.57.001171.

Bozinovic, N., Yue, Y., Ren, Y., Tur, M., Kristensen, P., Huang, H., Willner, A.E., Ramachandran, S., 2013. Terabit-scale orbital angular momentum mode division multiplexing in fibers. Science 340 (6140), 1545–1548. https://doi.org/10.1126/science:1237861.

Chen, L., Lei, J., Romero, J., 2014. Quantum digital spiral imaging. Light-Sci. Appl. 3 (3), e153. https://doi.org/10.1038/lsa:2014.34.

Chen, Y., Ni, R., Wu, Y., Du, L.i., Hu, X., Wei, D., Zhang, Y., Zhu, S., 2020. Phase-matching controlled orbital angular momentum conversion in periodically poled crystals. Phys. Rev. Lett. 125 (14) https://doi.org/10.1103/PhysRevLett.125.143901.

Coullet, P., Gil, L., Rocca, F., 1989. Optical vortices. Opt. Commun. 73 (5), 403–408. https://doi.org/10.1016/0030-4018(89)90180-6.
Courtial, J., Dholakia, K., Robertson, D.A., Allen, L., Padgett, M.J., 1998a. Measurement of the rotational frequency shift imparted to a rotating light beam possessing orbital angular momentum. Phys. Rev. Lett. 80 (15), 3217–3219. https://doi.org/10.1103/PhysRevLett.80.3217.
Courtial, J., Robertson, D.A., Dholakia, K., Allen, L., Padgett, M.J., 1998b. Rotational frequency shift of a light beam. Phys. Rev. Lett. 81 (22), 4828–4830. https://doi.org/10.1103/PhysRevLett.81.4828.
Cvijetic, N., Milione, G., Ip, E., Wang, T., 2015. Detecting lateral motion using light's orbital angular momentum. Sci. Rep. 5 (1) https://doi.org/10.1038/srep15422.
D'Ambrosio, V., Spagnolo, N., Del Re, L., Slussarenko, S., Li, Y., Kwek, L.C., Marrucci, L., Walborn, S.P., Aolita, L., Sciarrino, F., 2013. Photonic polarization gears for ultra-sensitive angular measurements. Nat. Commun. 4 (1) https://doi.org/10.1038/ncomms3432.
D'Errico, A., D'Amelio, R., Piccirillo, B., Cardano, F., Marrucci, L., 2017. Measuring the complex orbital angular momentum spectrum and spatial mode decomposition of structured light beams. Optica 4 (11), 1350. https://doi.org/10.1364/OPTICA.4.001350.
Dennis, M.R., O'Holleran, K., Padgett, M.J., 2009. Singular optics: optical vortices and polarization singularities//E. Wolf. Progr. Opt. 53, 293–363. https://doi.org/10.1016/s0079-6638(08)00205-9.
Emile, O., Emile, J., 2017. Naked eye picometer resolution in a michelson interferometer using conjugated twisted beams. Opt. Lett. 42, 354–357. https://doi.org/10.1364/ol.42.000354.
Fang, L., Padgett, M.J., Wang, J., 2017. Sharing a common origin between the rotational and linear doppler effects. Laser Photon. Rev. 11 (6), 1700183. https://doi.org/10.1002/lpor.201700183.
Fang, X., Wang, H., Yang, H., Ye, Z., Wang, Y., Zhang, Y., Hu, X., Zhu, S., Xiao, M., 2020. Multichannel nonlinear holography in a two-dimensional nonlinear photonic crystal. Phys. Rev. A 102 (4). https://doi.org/10.1103/PhysRevA.102.043506.
Fang, X., Yang, H., Yao, W., Wang, T., Zhang, Y., Gu, M., Xiao, M., 2021. High-dimensional orbital angular momentum multiplexing nonlinear holography. Adv. Photon. 3 (01) https://doi.org/10.1117/1.AP.3.1.01500110.1117/1.AP.3.1.015001.s01.
Fitzpatrick, C.A., Simon, D.S., Sergienko, A.V., 2014. High-capacity imaging and rotationally insensitive object identification with correlated orbital angular momentum states. Int. J. Quant. Inform. 12 (07n08), 1560013. https://doi.org/10.1142/S0219749915600138.
Franke-Arnold, S., Barnett, S.M., Yao, E., Leach, J., Courtial, J., Padgett, M., 2004. Uncertainty principle for angular position and angular momentum. New J. Phys. 6, 103. https://doi.org/10.1088/1367-2630/6/1/103.
Fürhapter, S., Jesacher, A., Bernet, S., Ritsch-Marte, M., 2005. Spiral phase contrast imaging in microscopy. Opt. Express 13 (3), 689. https://doi.org/10.1364/OPEX.13.000689.
Garetz, B.A., 1981. Angular doppler-effect. J. Opt. Soc. Am. 71, 609–611. https://doi.org/10.1364/josa.71.000609.
Garetz, B.A., Arnold, S., 1979. Variable frequency-shifting of circularly polarized laser-radiation via a rotating half-wave retardation plate. Opt. Commun. 31 (1), 1–3. https://doi.org/10.1016/0030-4018(79)90230-X.
Grier, D.G., 2003. A revolution in optical manipulation. Nature 424 (6950), 810–816. https://doi.org/10.1038/nature01935.
Guo, J., Guo, B., Fan, R., Zhang, W., Wang, Y.U., Zhang, L., Zhang, P., 2016. Measuring topological charges of laguerre-gaussian vortex beams using two improved mach-zehnder interferometers. Opt. Eng. 55 (3), 035104. https://doi.org/10.1117/1.OE.55.3.035104.
Jack B., 2011. Quantum entanglement of the spatial modes of light. University of Glasgow, 18-19. http://theses.gla.ac.uk/id/eprint/3017.
Jack, B., Padgett, M.J., Franke-Arnold, S., 2008. Angular diffraction. New J. Phys. 10 (10), 103013. https://doi.org/10.1088/1367-2630/10/10/103013.
Jha, A.K., Agarwal, G.S., Boyd, R.W., 2011. Supersensitive measurement of angular displacements using entangled photons. Phys. Rev. A 83 (5). https://doi.org/10.1103/PhysRevA.83.053829.
Jia, Q., Qiu, X., Wu, Z., Zhang, W., Chen, L., 2017. Transferring linear motion of an optical wedge to rotational frequency shift in an orbital angular momentum interferometer. Appl. Phys. Lett. 111 (9), 091102. https://doi.org/10.1063/1.4995366.
Karimi, E., Boyd, R.W., de la Hoz, P., de Guise, H., Řeháček, J., Hradil, Z., Aiello, A., Leuchs, G., Sánchez-Soto, L.L., 2014. Radial quantum number of laguerre-gauss modes. Phys. Rev. A 89 (6). https://doi.org/10.1103/PhysRevA.89.063813.
Kivshar, Y.S., Ostrovskaya, E.A., 2001. Optical vortices folding and twisting waves of light. Opt. Photon. News 12, 26–31. https://doi.org/10.1364/OPN.12.4.000024.
Kravets, V.G., Schedin, F., Jalil, R., Britnell, L., Gorbachev, R.V., Ansell, D., Thackray, B., Novoselov, K.S., Geim, A.K., Kabashin, A.V., Grigorenko, A.N., 2013. Singular phase nano-optics in plasmonic metamaterials for label-free single-molecule detection. Nat. Mater. 12 (4), 304–309. https://doi.org/10.1038/nmat3537.
Kruglov, V.I., Vlasov, R.A., 1985. Spiral self-trapping propagation of optical beams in media with cubic nonlinearity. Phys. Lett. A 111 (8-9), 401–404. https://doi.org/10.1016/0375-9601(85)90481-5.
Lavery, M.P.J., Speirits, F.C., Barnett, S.M., Padgett, M.J., 2013. Detection of a spinning object using light's orbital angular momentum. Science 341 (6145), 537–540. https://doi.org/10.1126/science:1239936.
Lee, J.H., Foo, G., Johnson, E.G., Swartzlander, G.A., 2006. Experimental verification of an optical vortex coronagraph. Phys. Rev. Lett. 97 (5) https://doi.org/10.1103/PhysRevLett.97.053901.
Li, F., Xu, T., Zhang, W., Qiu, X., Lu, X., Chen, L., 2018. Optical images rotation and reflection with engineered orbital angular momentum spectrum. Appl. Phys. Lett. 113 (16), 161109. https://doi.org/10.1063/1.5043229.
Ma, J., Wei, D., Wang, L., Zhang, Y., Xiao, M., 2021. High-quality reconstruction of an optical image by an efficient laguerre-gaussian mode decomposition method. Osa Contin. 4 (5), 1396. https://doi.org/10.1364/OSAC.419387.
Magaña-Loaiza, O.S., Mirhosseini, M., Cross, R.M., Rafsanjani, S.M.H., Boyd, R.W., 2016. Hanbury brown and twiss interferometry with twisted light. Sci. Adv. 2 (4), e1501143. https://doi.org/10.1126/sciadv.1501143.
Magaña-Loaiza, O.S., Mirhosseini, M., Rodenburg, B., Boyd, R.W., 2014. Amplification of angular rotations using weak measurements. Phys. Rev. Lett. 112 (20) https://doi.org/10.1103/PhysRevLett.112.200401.
Molina-Terriza, G., Rebane, L., Torres, J.P., et al., 2007. Probing canonical geometrical objects by digital spiral imaging. J. Eur. Opt. Soc. Rapid Publ. 2 https://doi.org/10.2971/jeos.2007.07014.
Naidoo, D., Roux, F.S., Dudley, A., et al., 2016. Controlled generation of higher-order poincare sphere beams from a laser. Nat. Photon. 10, 327-+. https://doi.org/10.1038/nphoton.2016.37.
Nye, J.F., Berry, M.V., 1974. Dislocations in wave trains. Proc. R. Soc. Lond. Ser. A-Mathemat. Phys. Eng. Sci. 336, 165–190. https://doi.org/10.1098/rspa.1974.0012.
O'Neil, A.T., MacVicar, I., Allen, L., Padgett, M.J., 2002. Intrinsic and extrinsic nature of the orbital angular momentum of a light beam. Phys. Rev. Lett. 88 (5) https://doi.org/10.1103/PhysRevLett.88.053601.
Qiu, S., Liu, T., Li, Z., Wang, C., Ren, Y., Shao, Q., Xing, C., 2019a. Influence of lateral misalignment on the optical rotational doppler effect. Appl. Opt. 58 (10), 2650. https://doi.org/10.1364/AO.58.002650.
Qiu, S., Liu, T., Ren, Y., Li, Z., Wang, C., Shao, Q., 2019b. Detection of spinning objects at oblique light incidence using the optical rotational doppler effect. Opt. Express 27 (17), 24781. https://doi.org/10.1364/OE.27.024781.
Richards, B., Wolf, E., 1959. Electromagnetic diffraction in optical systems.2. Structure of the image field in an aplanatic system. Proc. R. Soc. Lond. Ser. A-Mathemat. Phys. Sci. 253, 358–379. https://doi.org/10.1098/rspa.1959.0200.
Rogel-Salazar, J., Pablo, T.J., Chavez-Cerda, S., 2014. Engineering structured light with optical vortices. J. Opt. Soc. Am. B-Opt. Phys. 31, A46–A50. https://doi.org/10.1364/josab.31.000a46.
Shen, Y., Wang, X., Xie, Z., Min, C., Fu, X., Liu, Q., Gong, M., Yuan, X., 2019. Optical vortices 30 years on: Oam manipulation from topological charge to multiple singularities. Light-Sci. Appl. 8 (1) https://doi.org/10.1038/s41377-019-0194-2.
Simon, D.S., Sergienko, A.V., 2012. Two-photon spiral imaging with correlated orbital angular momentum states. Phys. Rev. A 85 (4). https://doi.org/10.1103/PhysRevA.85.043825.
Speirits, F.C., Barnett, S.M., 2013. Do waves carrying orbital angular momentum possess azimuthal linear momentum? Phys. Rev. Lett. 111 (10) https://doi.org/10.1103/PhysRevLett.111.103602.
Sroor, H., Huang, Y.-W., Sephton, B., Naidoo, D., Vallés, A., Ginis, V., Qiu, C.-W., Ambrosio, A., Capasso, F., Forbes, A., 2020. High-purity orbital angular momentum states from a visible metasurface laser. Nat. Photon. 14 (8), 498–503. https://doi.org/10.1038/s41566-020-0623-z.
Tamburini, F., Anzolin, G., Umbriaco, G., Bianchini, A., Barbieri, C., 2006. Overcoming the rayleigh criterion limit with optical vortices. Phys. Rev. Lett. 97 (16) https://doi.org/10.1103/PhysRevLett.97.163903.
Tamburini, F., Thidé, B.o., Molina-Terriza, G., Anzolin, G., 2011. Twisting of light around rotating black holes. Nat. Phys. 7 (3), 195–197. https://doi.org/10.1038/nphys1907.
Torner, L., Torres, J.P., Carrasco, S., 2005. Digital spiral imaging. Opt. Express 13, 873–881. https://doi.org/10.1364/opex.13.000873.
Uribe-Patarroyo, N., Fraine, A., Simon, D.S., Minaeva, O., Sergienko, A.V., 2013. Object identification using correlated orbital angular momentum states. Phys. Rev. Lett. 110 (4) https://doi.org/10.1103/PhysRevLett.110.043601.
Verma, G., Yadav, G., 2019. Compact picometer-scale interferometer using twisted light. Opt. Lett. 44, 3594–3597. https://doi.org/10.1364/ol.44.003594.
Wang, J., Yang, J.-Y., Fazal, I.M., Ahmed, N., Yan, Y., Huang, H., Ren, Y., Yue, Y., Dolinar, S., Tur, M., Willner, A.E., 2012. Terabit free-space data transmission employing orbital angular momentum multiplexing. Nat. Photon. 6 (7), 488–496. https://doi.org/10.1038/nphoton.2012.138.
Wei, D., Cheng, Y., Ni, R., Zhang, Y., Hu, X., Zhu, S., Xiao, M., 2019a. Generating controllable laguerre-gaussian laser modes through intracavity spin-orbital angular momentum conversion of light. Phys. Rev. Appl. 11 (1) https://doi.org/10.1103/PhysRevApplied.11.014038.
Wei, D., Ma, J., Wang, T., Xu, C., Zhu, S., Xiao, M., Zhang, Y., 2020. Laguerre-gaussian transform for rotating image processing. Opt. Express 28 (18), 26898. https://doi.org/10.1364/OE.403521.
Wei, D., Wang, C., Xu, X., Wang, H., Hu, Y., Chen, P., Li, J., Zhu, Y., Xin, C., Hu, X., Zhang, Y., Wu, D., Chu, J., Zhu, S., Xiao, M., 2019b. Efficient nonlinear beam shaping in three-dimensional lithium niobate nonlinear photonic crystals. Nat. Commun. 10 (1) https://doi.org/10.1038/s41467-019-12251-0.
Wei, D., Zhu, Y., Zhong, W., Cui, G., Wang, H., He, Y., Zhang, Y., Lu, Y., Xiao, M., 2017. Directly generating orbital angular momentum in second-harmonic waves with a spirally poled nonlinear photonic crystal. Appl. Phys. Lett. 110 (26), 261104. https://doi.org/10.1063/1.4990527.
Xiao, S., Zhang, L., Wei, D., Liu, F., Zhang, Y., Xiao, M., 2018. Orbital angular momentum-enhanced measurement of rotation vibration using a sagnac interferometer. Opt. Express 26 (2), 1997. https://doi.org/10.1364/OE.26.001997.
Xiao, Y.u., Tang, X., Wan, C., Qin, Y., Peng, H., Hu, C., Qin, B., 2019. Laguerre-gaussian mode expansion for arbitrary optical fields using a subspace projection method. Opt. Lett. 44 (7), 1615. https://doi.org/10.1364/OL.44.001615.

Xie, G., Liu, C., Li, L., Ren, Y., Zhao, Z., Yan, Y., Ahmed, N., Wang, Z., Willner, A.J., Bao, C., Cao, Y., Liao, P., Ziyadi, M., Almaiman, A., Ashrafi, S., Tur, M., Willner, A.E., 2017a. Spatial light structuring using a combination of multiple orthogonal orbital angular momentum beams with complex coefficients. Opt. Lett. 42 (5), 991. https://doi.org/10.1364/OL.42.000991.

Xie, G., Song, H., Zhao, Z., Milione, G., Ren, Y., Liu, C., Zhang, R., Bao, C., Li, L., Wang, Z., Pang, K., Starodubov, D., Lynn, B., Tur, M., Willner, A.E., 2017b. Using a complex optical orbital-angularmomentum spectrum to measure object parameters. Opt. Lett. 42 (21), 4482. https://doi.org/10.1364/OL.42.004482.

Yao, E., Franke-Arnold, S., Courtial, J., Barnett, S., Padgett, M., 2006. Fourier relationship between angular position and optical orbital angular momentum. Opt. Express 14 (20), 9071. https://doi.org/10.1364/OE.14.009071.

Zhai, Y., Fu, S., Zhang, R., Yin, C.i., Zhou, H., Zhang, J., Gao, C., 2019. The radial doppler effect of optical vortex beams induced by a surface with radially moving periodic structure. J. Opt. 21 (5), 054002. https://doi.org/10.1088/2040-8986/ab146f.

Zhang, C., Ma, L.U., 2017. Detecting the orbital angular momentum of electro-magnetic waves using virtual rotational antenna. Sci. Rep. 7 (1) https://doi.org/10.1038/s41598-017-04313-4.

Zhang, W., Gao, J., Zhang, D., He, Y., Xu, T., Fickler, R., Chen, L., 2018. Free-space remote sensing of rotation at the photon-counting level. Phys. Rev. Appl 10 (4). https://doi.org/10.1103/PhysRevApplied.10.044014.

Zhang, Y., Wang, T., Cheng, Y., Wei, D., Yao, W., Chen, P., Zhang, Y., Xiao, M., 2020. Controllable laser output of high-quality cylindrical vector beam through intra-cavity mode conversion. Appl. Phys. Lett. 117 (11), 111105. https://doi.org/10.1063/5.0020945.

Zhang, Z., Qiao, T., Ma, K., Cen, L., Zhang, J., Wang, F., Zhao, Y., 2016. Ultra-sensitive and super-resolving angular rotation measurement based on photon orbital angular momentum using parity measurement. Opt. Lett. 41 (16), 3856. https://doi.org/10.1364/OL.41.003856.

Zhou, H.-L., Fu, D.-Z., Dong, J.-J., Zhang, P., Chen, D.-X., Cai, X.-L., Li, F.-L., Zhang, X.-L., 2017. Orbital angular momentum complex spectrum analyzer for vortex light based on the rotational doppler effect. Light-Sci. Appl. 6 (4), e16251. https://doi.org/10.1038/lsa:2016.251.

Zhou, Z.-Y., Li, Y., Ding, D.-S., Zhang, W., Shi, S., Shi, B.-S., 2014a. Optical vortex beam based optical fan for high-precision optical measurements and optical switching. Opt. Lett. 39 (17), 5098. https://doi.org/10.1364/OL.39.005098.

Zhou, Z.-Y., Li, Y., Ding, D.-S., Zhang, W., Shi, S., Shi, B.-S., Guo, G.-C., 2014b. Highly efficient second harmonic generation of a light carrying orbital angular momentum in an external cavity. Opt. Express 22 (19), 23673. https://doi.org/10.1364/OE.22.023673.

Zhou, Z.-Y., Ding, D.-S., Jiang, Y.-K., Li, Y., Shi, S., Wang, X.-S., Shi, B.-S., 2014c. Orbital angular momentum light frequency conversion and interference with quasi-phase matching crystals. Opt. Express 22 (17), 20298. https://doi.org/10.1364/OE.22.020298.

Zhuang, X.W., 2004. Unraveling DNA condensation with optical tweezers. Science 305, 188–190. https://doi.org/10.1126/science.1100603.